A Centiparsec-scale Compact Radio Core in the Nearby Galaxy M60

Downloaded from: https://research.chalmers.se, 2026-10-15 05:09 UTC

Citation for the original published paper (version of record):
Li, X., Yang, J., Cheng, X. et al (2024). A Centiparsec-scale Compact Radio Core in the Nearby Galaxy M60. Astrophysical Journal, 960(1). http://dx.doi.org/10.3847/1538-4357/ad0be6

N.B. When citing this work, cite the original published paper.

research.chalmers.se offers the possibility of retrieving research publications produced at Chalmers University of Technology. It covers all kind of research output: articles, dissertations, conference papers, reports etc. since 2004. research.chalmers.se is administrated and maintained by Chalmers Library

(article starts on next page)

The Astrophysical Journal, 960:1 (11pp), 2024 January 1 https://doi.org/10.3847/1538-4357/ad0be6
© 2023. The Author(s). Published by the American Astronomical Society.
OPEN ACCESS

A Centiparsec-scale Compact Radio Core in the Nearby Galaxy M60

Xiaofeng Li[1,2,3], Jun Yang[4], Xiaopeng Cheng[5], Mai Liao[6,7,8], Xiaoyu Hong[9,10,11], Liming Dou[1,2,3], Tianle Zhao[1,2,3], Zhongying Fan[1,2,3], Fupeng Zhang[1,2,3], and Weirong Huang[1,2,3]
[1] Department of Astronomy, Guangzhou University, Guangzhou 510006, People's Republic of China; lixf@gzhu.edu.cn
[2] Great Bay Center, National Astronomical Data Center, Guangzhou, Guangdong 510006, People's Republic of China
[3] Astronomy Science and Technology Research Laboratory of Department of Education of Guangdong Province, Guangzhou 510006, People's Republic of China
[4] Department of Space, Earth and Environment, Chalmers University of Technology, Onsala Space Observatory, SE-439 92 Onsala, Sweden
[5] Korea Astronomy and Space Science Institute, Daedeok-daero 776, Yuseong-gu, Daejeon 34055, Republic of Korea; xcheng@kasi.re.kr
[6] National Astronomical Observatories, Chinese Academy of Sciences, 20A Datun Road, Chaoyang District, Beijing 100101, People's Republic of China
[7] Chinese Academy of Sciences South America Center for Astronomy, National Astronomical Observatories, CAS, Beijing 100101, People's Republic of China
[8] Instituto de Estudios Astrofísicos, Facultad de Ingeniería y Ciencias, Universidad Diego Portales, Av. Ejército 441, Santiago, Chile
[9] Shanghai Astronomical Observatory, Chinese Academy of Sciences, Shanghai 200030, People's Republic of China
[10] Shanghai Tech University, 100 Haike Road, Pudong, Shanghai 201210, People's Republic of China
[11] University of Chinese Academy of Sciences, 19A Yuquan Road, Beijing 100049, People's Republic of China
Received 2023 April 6; revised 2023 November 2; accepted 2023 November 9; published 2023 December 18

Abstract

M60, an elliptical galaxy located 16.5 Mpc away, has an active nucleus with a very low luminosity and an extremely low accretion rate. Its central supermassive black hole (SMBH) has a mass of $M_{\rm BH} \sim 4.5 \times 10^9\,M_\odot$ and a Schwarzschild radius corresponding to $R_{\rm S} \sim 5.4\,\mu$as. To investigate the nature of its innermost radio nucleus, data from the Very Long Baseline Array (VLBA) at 4.4 and 7.6 GHz were reduced. The VLBA images reveal a compact component with total flux densities of ∼20 mJy at both frequencies, a size of $\leqslant$0.27 mas (99.7% confidence level), about 0.022 pc (50 $R_{\rm S}$) at 7.6 GHz, and a brightness temperature of $\geqslant 6 \times 10^9$ K. This suggests that the observed centiparsec-scale compact core could be attributed to a nonthermal jet base or an advection-dominated accretion flow (ADAF) with nonthermal electrons. The extremely compact structure also supports the presence of an SMBH in the center. Our results indicate that M60 is a promising target for broadband very long baseline interferometry observations at millimeter wavelengths to probe ADAF scenarios and tightly constrain the potential photon ring (about 28 μas) around its SMBH.

Unified Astronomy Thesaurus concepts: Supermassive black holes (1663); Low-luminosity active galactic nuclei (2033); Schwarzschild radius (1435); Very long baseline interferometry (1769); Radio cores (1341); Jets (870); Galaxy accretion disks (562)

1. Introduction

Spectroscopy and dynamical modeling suggest that supermassive black holes (SMBHs) are usually located in the center of massive galaxies (Gebhardt et al. 2000; Kormendy & Ho 2013). The most powerful evidence for the presence of an SMBH in the center of a galaxy is the detection of the inner radio structure close to the SMBH candidates, e.g., M87 (EHT Collaboration et al. 2019), Sagittarius A* (Sgr A*; EHT Collaboration et al. 2022), and NGC 4258 (Miyoshi et al. 1995). A spectroscopic survey of nearby bright galaxies found that around 40% of them contain low-luminosity active galactic nuclei (LLAGNs) that are powered by SMBHs (Ho et al. 1997; Ho 2008). Generally, the radiation of most LLAGNs originates from subparsec-scale or even smaller regions, making it difficult for radio observations to resolve these regions. The radiation mechanism of LLAGNs is not yet well understood.

Radio images of LLAGNs often display a compact core, and some of them also have jetlike structures (Ho & Ulvestad 2001; Nagar et al. 2005). These radio cores remain compact on milliarcsecond scales, as observed through very long baseline interferometry (VLBI; e.g., Ulvestad et al. 1999; Falcke et al. 2000; Ulvestad & Ho 2001; Nagar et al. 2002, 2005; Anderson et al. 2004; Doi et al. 2005; Park et al. 2017). A few LLAGNs have been resolved on scales of $\leqslant$100 Schwarzschild radii, $R_{\rm S}$, including Sgr A* (Shen et al. 2005; Lu et al. 2018; EHT Collaboration et al. 2022), M87 (Hada et al. 2011; EHT Collaboration et al. 2019; Lu et al. 2023), Cen A (Janssen et al. 2021), M104 (Hada et al. 2013), M81 (Jiang et al. 2018), and M84 (Jiang et al. 2021). The radio cores of LLAGNs typically have a flat or slightly inverted spectrum (Ho & Ulvestad 2001; Anderson et al. 2004; Nagar et al. 2005; Cho et al. 2022). The LLAGN jets usually have subluminal speeds (Ulvestad et al. 1999; Hada et al. 2013).

The radio emission of LLAGNs has multiple origins, one of the most common being outflows. These outflows consist of collimated jets (Blandford & Znajek 1977; Falcke & Biermann 1999; Chen & Zhang 2021), accelerated to relativistic velocities (Lister et al. 2021) with a very small opening angle (Pushkarev et al. 2017), and winds (Blandford & Payne 1982; Blandford & Begelman 1999) with low brightness, a large opening angle, and low velocity (Panessa et al. 2019). The jets emit a power-law continuum spectrum in the radio band, which is caused by nonthermal synchrotron radiation. Radio winds have the same radiation mechanism as jets but are much weaker than jets due to low energy and weak magnetic fields. They have only been detected in a few sources, e.g., Mkr 6 (Kharb et al. 2006, 2014). Additionally, advection-dominated accretion flows (ADAFs), known as geometrically thick and optically thin, also emit significant radio flux

Original content from this work may be used under the terms of the Creative Commons Attribution 4.0 licence. Any further distribution of this work must maintain attribution to the author(s) and the title of the work, journal citation and DOI.

(Narayan & Yi 1994, 1995; Yuan et al. 2003). The radio emission from ADAF primarily dominates in the very inner region, making it difficult to study with low-resolution observations (Mahadevan 1997; Manmoto et al. 1997; Bandyopadhyay et al. 2019). Lastly, star formation activity and supernova remnants can also contribute significant radio emission, adding complexity to the study of outflow and ADAF (Panessa et al. 2019).

Sgr A*, the closest known SMBH at a distance $D \sim 8.1$ kpc (GRAVITY Collaboration et al. 2019), is one of the most promising targets for studying the vicinity of SMBHs at extremely low accretion rates (EHT Collaboration et al. 2022). Despite extensive VLBI observations, no direct evidence of a jet has been found in Sgr A* (Rauch et al. 2016; Cho et al. 2022; EHT Collaboration et al. 2022; Cheng et al. 2023). Interstellar scattering (Bower et al. 2006; Psaltis et al. 2018) is a major obstacle to detecting potential jets in Sgr A*. To avoid complications caused by interstellar scattering, we conducted a comprehensive literature review (e.g., Kormendy & Ho 2013; Ramakrishnan et al. 2023) and identified M60 as a prime candidate for studying the presence of jets in LLAGNs with very low luminosity and extremely low accretion rates.

M60 (NGC 4649), a nearby elliptical galaxy, has an active nucleus (Di Matteo & Fabian 1997; Di Matteo et al. 1999; Paggi et al. 2017). Its high Galactic latitude ($b = 74.^{\circ}3$) implies that the interstellar medium has a negligible effect on scatter broadening (Koryukova et al. 2022). The distance to M60, as estimated by the tip of the red giant branch method, is $d = 16.23 \pm 0.50(\mathrm{ran}) \pm 0.42(\mathrm{sys})$ Mpc (Lee & Jang 2017), and the surface brightness fluctuation method gives an estimate of $d = 16.7 \pm 0.6$ Mpc (Cantiello et al. 2018). In this work, we use the weighted average of the two distances, $d = 16.5 \pm 0.5$ Mpc. The image scale of M60 is 0.080 ± 0.003 pc mas^{-1}. The central object, most likely an SMBH, has a dynamic mass of $M_{\mathrm{BH}} = (4.5 \pm 1.0) \times 10^9 M_{\odot}$ (scaled to solar mass, black hole mass represented by $m = (4.5 \pm 1.0) \times 10^9$; Shen & Gebhardt 2010). The central SMBH candidate has an angular size of $R_{\mathrm{S}} = 2GM_{\mathrm{BH}}/(c^2 d) \sim 5.4$ μas, where G and c are the gravitational constant and the speed of light, respectively. The mass accretion rate of an SMBH $\dot{M}$ is often scaled to Eddington rate $\dot{M}_{\mathrm{Edd}} = 10 L_{\mathrm{Edd}}/c^2$, i.e., $\dot{m} = \frac{\dot{M}}{\dot{M}_{\mathrm{Edd}}}$, where L_{Edd} is the Eddington luminosity.[12] The scaled mass accretion rate of M60, as reported by Johannsen et al. (2012), is $\dot{m} = 1.4 \times 10^{-8}$, and Paggi et al. (2014) reported a rate of $\dot{m} = 7.2 \times 10^{-9}$. Both of these accretion rates are extremely low. We adopt the arithmetic mean value of these two scaled mass accretion rates, $\dot{m} \sim 1.1 \times 10^{-8}$, for this study. Given the relatively large angular size of R_{S} in M60, this galaxy may provide an excellent opportunity to study the properties of ADAF and jets in LLAGNs with very low mass accretion rates using VLBI observations.

The Very Large Array (VLA; Stanger & Warwick 1986; Grossová et al. 2022; Temi et al. 2022) and Low-Frequency Array (Capetti et al. 2022) images of M60 exhibit a typical Fanaroff–Riley type I (Fanaroff & Riley 1974) radio galaxy morphology on kiloparsec scales, which includes a compact core and double side jets. These jets are also associated with X-ray cavities (Shurkin et al. 2008; Dunn et al. 2010; Paggi et al. 2014). The high-resolution VLA A-configuration images (Grossová et al. 2022; Temi et al. 2022) or high-frequency images (Di Matteo et al. 1999) of M60 only display a compact core. Submillimeter Array (SMA) observations detected significant variability at 223 GHz in M60 in 2016 March (Lo et al. 2023). The radio flux density of M60 at 223 GHz varied from nondetection ($\leqslant$8.1 mJy) on March 3, increasing to 15.9 ± 2.1 mJy on March 5, and then decreasing to 6.7 ± 1.6 mJy on March 13. Infrared observations and dust absorption maps suggest that M60 is a cold gas–free galaxy with no signs of star formation (Temi et al. 2022). Thus, it could be an ideal candidate for VLBI observations to investigate outflow or ADAF radio emission properties. Furthermore, VLBI observations could provide more direct evidence for the presence of an accreting SMBH in M60 (e.g., Maoz 1995, 1998; Genzel et al. 2000; Ghez et al. 2005; Shen et al. 2005) and independently constrain its SMBH mass (Johannsen & Psaltis 2010; Johannsen et al. 2012).

This paper is structured as follows. In Section 2, we introduce the radio data used, which include high-resolution Very Long Baseline Array (VLBA) data and low-resolution archival radio flux density. Section 3.1 presents the imaging results, and Section 3.2 discusses the radio origins of the compact component. Section 3.3 provides independent evidence supporting the presence of an SMBH in M60. Finally, Section 4 summarizes the conclusions.

2. Data Reduction and Analysis

2.1. VLBA Observations and Data Reduction

In the VLBA Calibrator Survey 12 (program code BP252AF; principal investigator: Leonid Petrov), the radio AGN in M60 was observed simultaneously at 4.4 and 7.6 GHz for a duration of 3 minutes on 2022 July 26. During the experiment, the stations Kitt Peak and North Liberty (NL) were out, and the station Pie Town (PT) failed to record data. As a result, seven VLBA stations contributed valid data. The experiment was carried out with circular right polarization at a data rate of 4096 Mbps using eight subbands (four at 4.4 GHz and four at 7.6 GHz), 128 MHz subband^{-1}, and 2-bit quantization. The DiFX2 software correlator (Deller et al. 2011) at the National Radio Astronomy Observatory (NRAO) was employed to correlate the data utilizing a 0.0625 MHz frequency resolution and a 0.1 s integration time.

The correlation data were calibrated in the Astronomical Image Processing System (AIPS, version 31DEC21; Greisen 2003). After the data were imported into AIPS, we corrected the correlation amplitudes due to minor sampling errors and then ran amplitude calibration based on the system temperature data and antenna gain curves. NRAO recently announced that the default antenna gain values of PT and NL at the C band (4–8 GHz) between 2020 February 11 and 2023 April 5 were incorrect due to incorrect focus. To fix the issue, we used the new gain curve table provided by NRAO.[13] To align phases across subbands, we performed fringe fitting on the 1 minute data from the ~1 Jy bright calibrator B1116+128. After the manual phase calibration, we merged the subbands in halves (i.e., the 4.4 and 7.6 GHz data are combined, respectively) to enhance the signal-to-noise ratio (S/N) of the solution and conducted global fringe fitting on the data of M60

[12] The Eddington luminosity is the maximum luminosity that can be achieved by an accreting black hole when there is hydrostatic equilibrium: $L_{\mathrm{Edd}} = 4\pi G M_{\mathrm{BH}} c m_p/\sigma_{\mathrm{T}}$, where σ_{T} is the Thomson cross section and m_p is the mass of a proton.

[13] https://science.nrao.edu/facilities/vlba/data-processing/vlba-7ghz-flux-density-scale

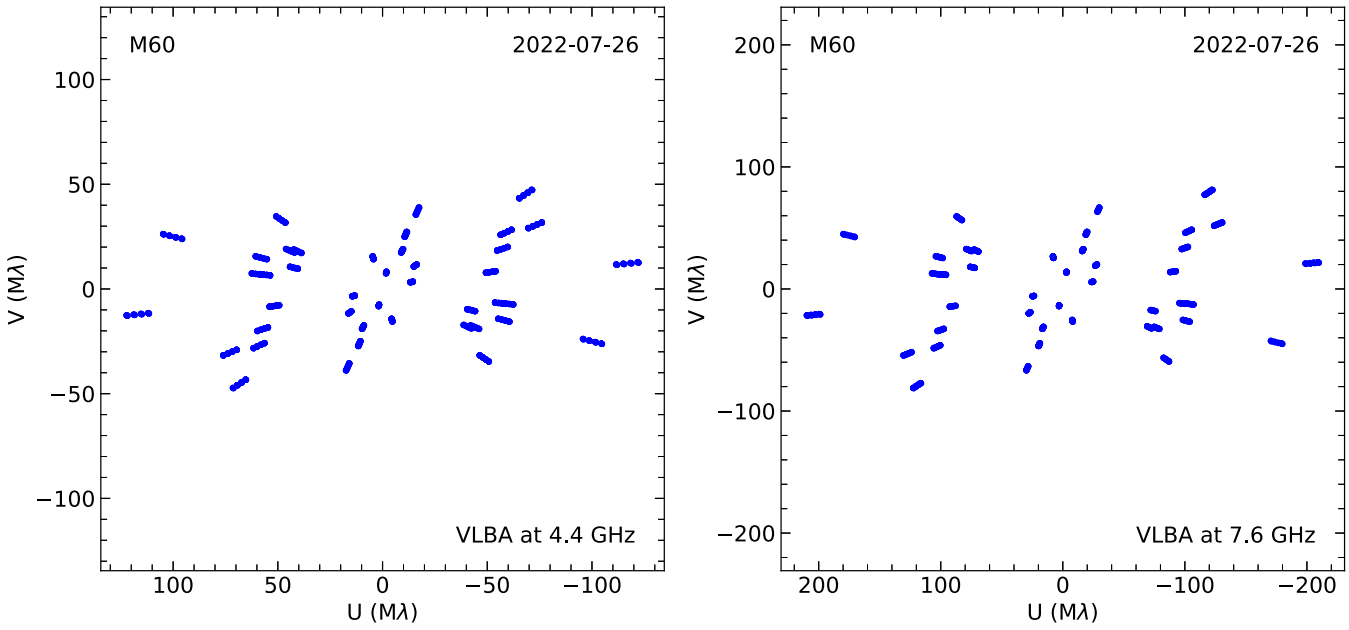

Figure 1. The (u, v) coverage for M60 at 4.4 GHz (left) and 7.6 GHz (right). The (u, v) coordinates for each pair of antennas are the baseline length projected from the source in units of the observing wavelength λ and are given for conjugate pairs.

with a 0.75 minute solution interval. All the solutions had S/Ns greater than 4. Finally, we applied all the solutions to the data, averaged all the frequency channels in each subband, and split the data at 4.4 and 7.6 GHz into two files.

The (u, v) coverage of M60 is shown in Figure 1. The 4.4 and 7.6 GHz data have similar characteristics, with sparse (u, v) coverage. The maximum side lobe was approximately 72% of the primary lobe.

The radio source M60 is relatively weak (correlation amplitude ∼20 mJy). Before running the amplitude self-calibration on the M60 data, we also did a test to verify the reliability of the step. In the same geodetic VLBI experiment, the compact calibrator B1241+166 with a total flux density of ∼380 mJy at 4.4 GHz was also observed. Because both M60 and B1241+166 have a small separation of 4°.8 and were observed in two neighboring scans, their data were supposed to suffer fairly consistent amplitude errors. We did deconvolution and self-calibration on the data of the pair of sources in `Difmap`. The amplitude self-calibration solutions looked quite similar and were fully as expected. Therefore, it is safe to run the self-calibration of amplitude on the data of M60.

In view of the positive results above, we transferred the amplitude self-calibration solutions from the bright calibrator B1241+166 to the nearby target M60 in `AIPS`. The gain correction factors of B1241+166, derived from the `gscale` command in `Difmap` (Shepherd 1997), are reported in Appendix A. We noticed that the gain correction factors of the station Los Alamos (LA) were abnormally larger than those of other stations. After contacting VLBA support scientists, we figured out that these large correction factors resulted from improper antenna gain measurements.

After calibrating out the large amplitude errors with the nearby bright calibrator B1241+166 in `AIPS`, we did deconvolution and self-calibration in `Difmap`. Initially, we fitted the circular Gaussian model to the visibility data and then performed phase self-calibration with a solution interval of 1.5 minutes. After a few iterations, we started to run the amplitude self-calibration. The amplitude correction factors of M60 were also listed in Appendix A. All the correction factors are quite close to 1, in particular at 4.4 GHz. The `selfcal` command was then run with a solution interval of 3 minutes, allowing the amplitude and phase to change simultaneously. The model fitting and self-calibration processes were repeated until the reduced chi-square χ^2_ν was minimized. To obtain accurate uncertainty estimates, we scaled the data weights to set $\chi^2_\nu = 1$. The data at 4.4 and 7.6 GHz were reduced with the same method. We also tried the elliptical Gaussian model. Because some best-fitting parameters, in particular the position angle of the major axis, had large uncertainties, the more complex model was not considered in the paper. The final clean images of M60 at 4.4 and 7.6 GHz are presented in Figure 2.

To accurately characterize the uncertainties of the parameters of the Gaussian model, in particular the angular size, we also used the Markov Chain Monte Carlo (MCMC) method to fit the circular Gaussian mode to the visibility data calibrated in `Difmap`. The used MCMC program `MCMCUVFit` was developed by us. More details of the program are available in Appendix B. The results of the MCMC method are presented in Table 1. The calibrated visibility and the model from the MCMC output are shown in the right panels of Figure 2.

We also tried the MCMC and least-squares fitting methods to analyze the M60 visibility data using phase-only self-calibration in `Difmap`. The best-fitting parameters show slightly larger uncertainties but are fully consistent with the above results using the phase and amplitude self-calibration.

2.2. Nonsimultaneous Radio Spectrum

To analyze the origin of the radio emission in M60, we collected radio flux density measurements in some online data archives and literature. To exclude possible diffuse emission from the relic jet, we used the measurements from the VLBA data and the VLA data observed with the A configuration at $\leqslant$15 GHz. At higher frequencies, the contribution of the extended steep spectrum relic jet is quite low and can be ignored. Therefore, we included low-resolution data. The VLBA data are the first

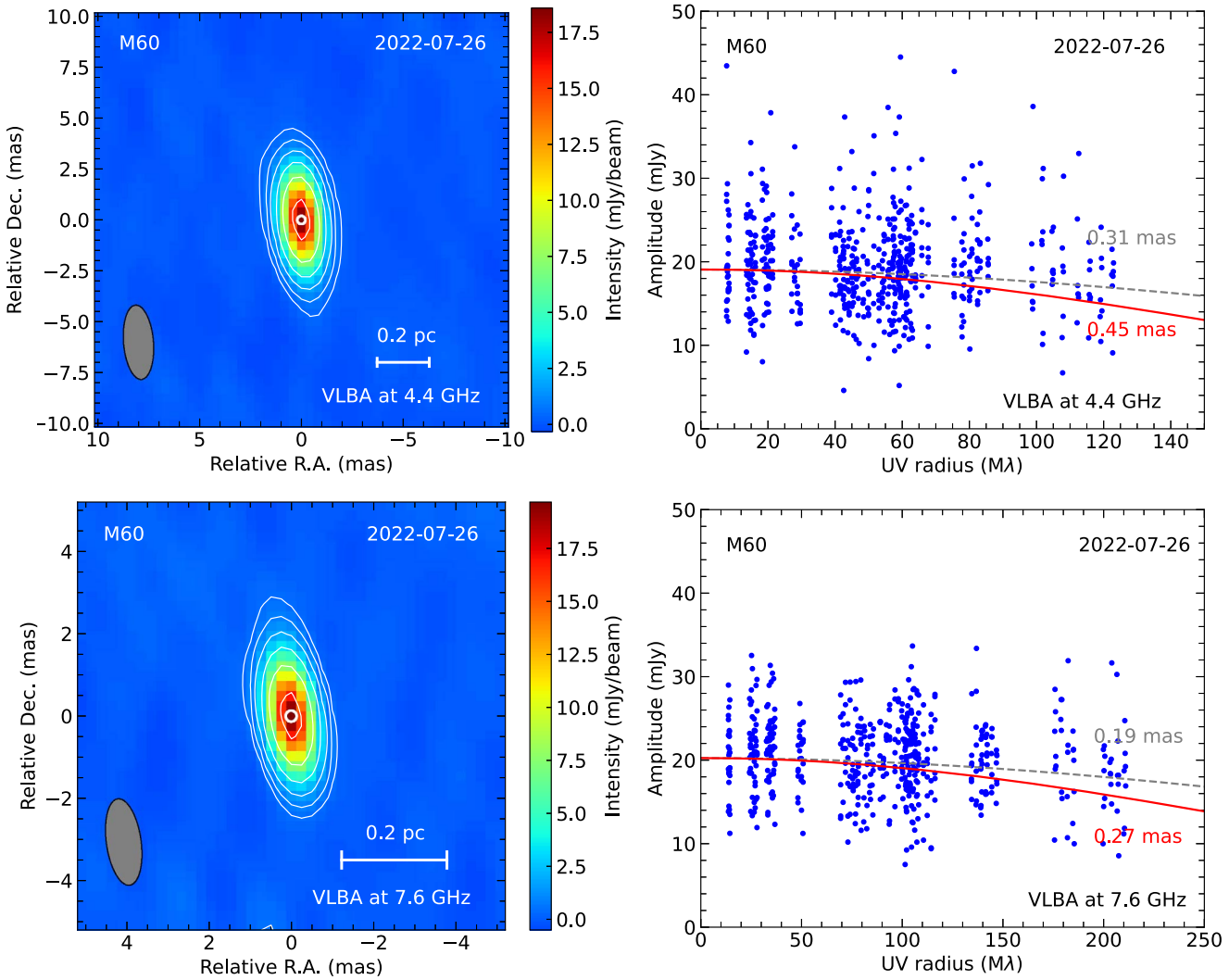

Figure 2. The VLBA CLEAN images (left) and observed visibility (right) of M60 (NGC 4649). The top panels are 4.4 GHz results, while the bottom panels are 7.6 GHz results. The peak brightness of the 4.4/7.6 GHz image is 18.83/17.40 mJy beam^{-1}. The rms of the 4.4/7.6 GHz image is 0.16/0.17 mJy beam^{-1}. The contour levels of the 4.4/7.6 GHz image are 0.48/0.51 mJy beam^{-1} × (−1, 1, 2, 4, 8, 16), and the color bar is in mJy beam^{-1}. The beam FWHM of the 4.4 GHz image is 3.68 × 1.50 mas at 6°.11, and the beam FWHM of the 7.6 GHz image is 2.12 × 0.86 mas at 7°.28. The thick white lines at the image center represent the upper limit (99.7% confidence) of the deconvoluted angular size. The correlation amplitude is vs. the radius in the (u, v) plane. The visibility data were calibrated. The gray dashed and red solid lines represent the models using the angular sizes at 50% and 99.7% confidence levels.

VLBI detected flux density that is presented in Appendix B. Most data are extracted from the NRAO VLA Archive Survey (NVAS; Crossley et al. 2008).[14] M60 was observed by the Atacama Large Millimeter/submillimeter Array (ALMA) at ∼350 GHz to study its black hole mass, central parsec gas dynamics, and event horizon detectability by CO lines (program codes 2016.1.01135.S and 2017.1.00830.S; principal Investigator: Neil Nagar). Temi et al. (2022) reported nondetection of the CO lines. We reduced these ALMA data to extract flux densities from the radio continuum spectrum. The data reduction was carried out in Common Astronomy Software Applications (CASA) casa-release-5.1.1 (McMullin et al. 2007) with ALMA Pipeline-Cycle5-R2-B (ALMA Pipeline Team 2017). The resulting radio flux density of M60 at 350 GHz is 1.7 ± 0.2 mJy on 2017 July 18 and 1.1 ± 0.1 mJy on 2017 December 24. We also include four published data points: one data point was observed by the VLA with the A configuration at 1.5 (Grossová et al. 2022; Temi et al. 2022), two data points were observed by the VLA with the D configuration at 22 and 43 GHz (Di Matteo et al. 1999), and one data point was observed by the Submillimeter Common-User Bolometric Array (SCUBA) at 150 GHz (Di Matteo et al. 1999). These error bars include systematic errors: 5% for the VLBA results and 3% for the VLA results. All these flux density measurements are presented in Table 2. There is no hint of strong variability from these nonsimultaneous observations, which span approximately four decades, except the SMA data, which are not used.

3. Results and Discussion

3.1. Radio Images of M60

Recently, the Astrogeo Center precisely determined the location of the radio source in M60. According to the Radio Fundamental Catalog (RFC),[15] which is available to the public, the coordinates are R.A. = 12:43:39.9715 and

[14] https://www.vla.nrao.edu/astro/nvas/

[15] http://astrogeo.org/rfc/

Table 1
VLBI Results of M60 at the *C* Band

ν (GHz) (1)	Beam (mas×mas, deg) (2)	S_p (mJy beam^{-1}) (3)	rms (mJy beam^{-1}) (4)	S_{tot} (mJy) (5)	θ_{core} (mas/R_S) (6)	x (mas) (7)	y (mas) (8)
4.4	3.65 × 1.46, 4.69	18.58	0.16	19.1 ± 1.0	⩽0.45/⩽83	$0.008^{+0.006}_{-0.006}$	$0.015^{+0.015}_{-0.015}$
7.6	2.11 × 0.84, 7.99	19.69	0.17	20.2 ± 1.0	⩽0.27/⩽50	$0.007^{+0.004}_{-0.004}$	$0.008^{+0.009}_{-0.009}$

Note. Column 1: observation frequency in GHz. Column 2: restore beam shape (major and minor axes in mas, position angle in deg). Column 3: peak flux density in mJy beam^{-1}. Column 4: image rms in mJy beam^{-1}. Column 5: total flux density in mJy. Column 6: core size in mas or R_S with 99.7% confidence. Columns 7 and 8: position relative to image center in mas.

Table 2
Radio Flux Density for Continuum Spectrum Fitting

Telescope	Epoch (YYYY-MM-DD)	ν (GHz)	S_ν (mJy)	Reference
VLA/A	1982-04-04	1.5	16.7 ± 0.5	NVAS
VLA/A	1982-04-04	4.9	15.5 ± 0.5	NVAS
VLA/A	1982-04-04	15	17.7 ± 0.5	NVAS
VLA/A	1984-12-15	4.9	19.7 ± 0.6	NVAS
VLA/A	1991-08-25	1.5	14.4 ± 0.4	T22, G22
VLA/D	1997-12-07	22	23.5 ± 0.7	D99
VLA/D	1997-12-07	43	12.9 ± 0.4	D99
SCUBA	1998-01-30	150	⩽5.1	D99
VLA/C	1998-12-30	22	22.3 ± 0.7	NVAS
VLA/C	1998-12-30	43	21.3 ± 0.6	NVAS
ALMA	2017-07-18	350	1.7 ± 0.2	This work
ALMA	2017-12-24	350	1.1 ± 0.1	This work
VLBA	2022-07-26	4.4	19.1 ± 1.0	This work
VLBA	2022-07-26	7.6	20.2 ± 1.0	This work

Note. Column 1: telescope. Column 2: epoch. Column 3: observation frequency in GHz. Column 4: flux density in mJy. Column 5: references: NVAS, Crossley et al. (2008); T22, Temi et al. (2022); G22, Grossová et al. (2022); D99, Di Matteo et al. (1999).

decl. = +11:33:09.688 (with an error of 1.8 mas). In Gaia Data Release 3 (DR3), the optical coordinates of M60 are given as R.A. = 12:43:39.9708 (with an error of 6.2 mas) and decl. = +11:33:09.6882 (with an error of 2.8 mas; Gaia Collaboration et al. 2022). The RFC position of M60 is located east of the Gaia DR3 position, with a separation of 9.9 mas. This indicates that the radio position is consistent with the optical position.

The left panels of Figure 2 display the total intensity images of M60 at 4.4 and 7.6 GHz. The peak brightness of the 4.4/7.6 GHz image is 18.58/19.69 mJy beam^{-1}, and the image rms is 0.16/0.17 mJy beam^{-1}, respectively. The image scale is 0.08 pc mas^{-1}, and the average beam size at 4.4/7.6 GHz is 2.31/1.33 mas. The total flux density at 4.4 and 7.6 GHz is 19.1 ± 1.0 and 20.2 ± 1.0 mJy, respectively, with the error mainly due to the systematic error (5%). The radio component remains unresolved, with an upper limit size of ⩽0.45 mas (0.036 pc, or 83 R_S) at 4.4 GHz and ⩽0.27 mas (0.022 pc, or 50 R_S) at 7.6 GHz at a confidence level of 99.7%. These sizes are roughly one-fifth of the restore beam. The fitted component sizes at both bands are on centiparsec scales. The relatively low image sensitivity did not allow us to detect the emission beyond the compact core, and the subparsec-scale jet might be resolved out or substantially weaker than the image sensitivity can detect.

The VLBA data of M60 suggest a spectral index of $\alpha^{7.6\,\mathrm{GHz}}_{4.4\,\mathrm{GHz}} = 0.11 \pm 0.13$ ($S_\nu \propto \nu^{+\alpha}$), implying a slightly inverted spectrum at 4.4–7.6 GHz. Figure 3 displays the nonsimultaneous radio spectrum of M60, which is marginally inverted at ⩽21.6 GHz with $\alpha_{thick} = 0.12 \pm 0.04$ and steep at >21.6 GHz with $\alpha_{thin} = -1.5 \pm 0.1$ (see Section 3.2.1). The brightness temperatures of the unresolved component are $T_B(4.4\,\mathrm{GHz}) \geqslant 6.0 \times 10^9$ and $T_B(7.6\,\mathrm{GHz}) \geqslant 5.9 \times 10^9$ K, which is much higher than the typical brightness temperature of thermal radiation ($\leqslant 10^5$ K).

The morphology of M60 on both kiloparsec and centiparsec scales, its slightly inverted radio spectrum, and its extremely high brightness temperature all point to the radio emission being caused by an AGN rather than star formation. This is further supported by the lack of cold gas, which is necessary for star formation, as evidenced by the nondetection of [C II]-emitting gas with SOFIA, the nondetection of a CO line by ALMA, and the absence of dust in the Hubble Space Telescope dust absorption map (Temi et al. 2022).

3.2. Origin of the Centiparsec-scale Compact Component

In the vicinity of LLAGN SMBHs, radio emission could be generated by outflows such as jets (Blandford & Znajek 1977; Falcke & Biermann 1999; Chen & Zhang 2021) and winds (Blandford & Payne 1982; Blandford & Begelman 1999) or an ADAF (Narayan & Yi 1994; Mahadevan 1997; Manmoto et al. 1997). However, in the case of M60, no extended jets or winds exceeding 0.85 mJy beam^{-1} were detected in the VLBI images. Therefore, we only consider two possible origins: the jet base and the ADAF. Both of these origins have a peaked continuum spectrum in the radio bands. The jet base has an inverted spectrum at low frequency with a spectral index of $0 < \alpha \leqslant 2.5$ and a steep spectrum at high frequency (Falcke & Biermann 1999). On the other hand, the ADAF has a similar continuum spectrum but with a spectral index of $\alpha \sim 0.4$ at low frequency (Mahadevan 1997). A comprehensive analysis of these possibilities is provided in the following sections.

3.2.1. Jet Base

The radio continuum spectrum of M60 is shown in Figure 3. To measure the variability of M60, we employ the variability index $m_{var} = \sigma/\langle S \rangle$, where $\langle S \rangle$ and σ are the mean and standard deviation of the flux density, respectively. The m_{var} at 1.5 and 4.9 GHz is approximately 7.4% and 11.9%, respectively, indicating a low variability. The radio flux density at 223 GHz detected by SMA showed significant variability during 2016 March (Lo et al. 2023) but was not used in the continuum spectrum fitting. The M60 radio spectrum is characterized by a peaked shape, which can be attributed to

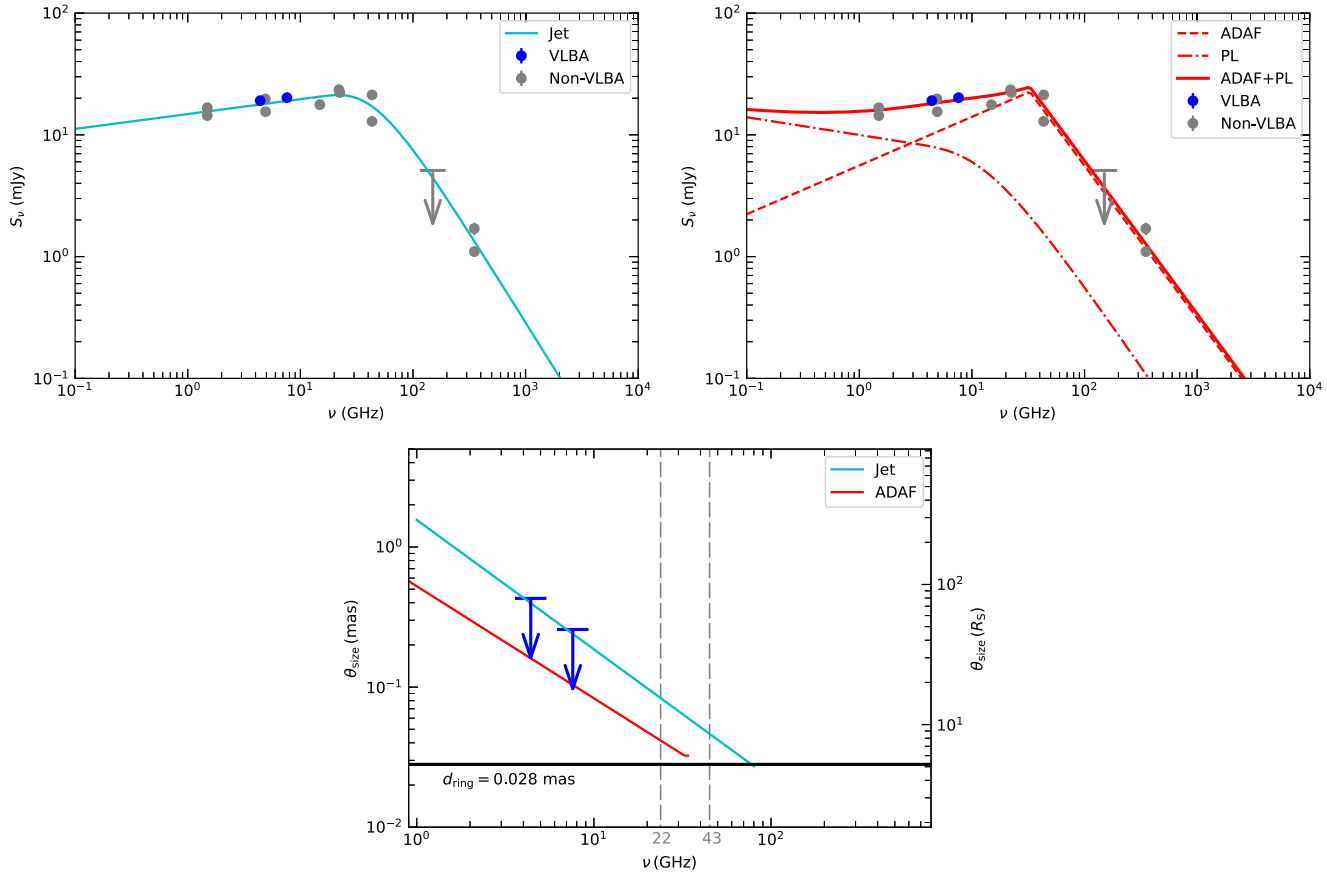

Figure 3. The nonsimultaneous radio spectrum and the observed angular sizes of M60. Top left: the gray and blue filled circles represent the non-VLBA and VLBA data, respectively. The cyan solid line depicts the best-fitting results from a peaked spectrum of jet base emission. Top right: the radio spectrum is fitted to a model composed of an ADAF component and a power-law component. The red dashed and dashed–dotted lines represent the contribution from the ADAF and power-law components, respectively. The total flux density is shown by the red solid line. Bottom: the blue arrows indicate the upper limit of the observed angular size. The black solid horizontal line predicts the photon ring diameter based on the dynamics mass of the SMBH. The gray dashed vertical lines indicate the available VLBI observing frequencies close to the peak frequency. The cyan solid line represents the core size predicted by a jet model with a characteristic electron Lorentz factor of $\gamma_{e,0} = 230$. The core size predicted by the ADAF model, which only has thermal electrons, is shown by the red solid line.

the synchrotron radiation of jets (Konigl 1981; Chen 2017). Inverted and steep spectral indexes indicate the optically thick and thin parts, respectively. To fit the radio spectrum of M60, we use a smooth broken power-law (BPL) model proposed by Callingham et al. (2017). The flux density S_ν is given by

$$S_\nu = \frac{S_t}{1 - e^{-1}}(1 - e^{-(\nu/\nu_t)^{\alpha_{thin}-\alpha_{thick}}})\left(\frac{\nu}{\nu_t}\right)^{\alpha_{thick}}, \quad (1)$$

where α_{thick} and α_{thin} are the spectral indexes in the optically thick and optically thin regions, respectively, and S_t is the flux density at the turnover frequency ν_t. The data used to fit are presented in Table 2, and a variable error of 10% ($\sigma_{var} = 10\% \times S_{tot}$) was added to the flux density error, i.e., $\sigma = \sqrt{\sigma_m^2 + \sigma_{var}^2}$, where σ_m is the measurement error. The fitting results are $\nu_t = 51^{+8}_{-7}$ GHz, $S_t = 15^{+1}_{-1}$ mJy, $\alpha_{thick} = 0.12^{+0.04}_{-0.04}$, and $\alpha_{thin} = -1.5^{+0.1}_{-0.1}$. The flux density of the model is plotted with a cyan solid line in Figure 3 (top left). It is important to note that ν_t is not the peak frequency but the turnover frequency. The peak frequency ν_p and peak flux density S_p can be numerically derived from model parameters. By substituting the parameters of the fit into Equation (1), we obtain $\nu_p \sim 21.6$ GHz and $S_p \sim 21.2$ mJy.

Equation (8) in Falcke & Biermann (1999) can be used to determine the jet power Q_{jet} and the inclination angle i of the jet in relation to the line of sight. The characteristic electron Lorentz factor of the jet, denoted as $\gamma_{e,0}$, is a free parameter. We set it to $\gamma_{e,0} = 230$, which is lower than the median value of 300, to ensure that the simulated jet size is in line with the core size–frequency relation (Figure 3, bottom). This yields an estimated jet power of $Q_{jet} \sim 5.7 \times 10^{41}$ erg s^{-1} and an inclination angle of $i \sim 30°$.

3.2.2. ADAF

The low luminosity (Di Matteo & Fabian 1997; Di Matteo et al. 1999; Paggi et al. 2014) and low accretion rate (Johannsen et al. 2012; Paggi et al. 2014) of M60 suggest that its accretion disk is an ADAF, which exhibits radio emission in the inner disk region. This ADAF model has a peaked spectrum with an inverted spectral index of approximately 0.4 before the peak frequency, which is due to synchrotron cooling, and a steep spectral index after the peak frequency, which is caused by Compton cooling (Mahadevan 1997; Manmoto et al. 1997). Mahadevan (1997) provided an analytical expression for the ADAF radiation spectrum by a self-similar solution, which can accurately describe the main features of ADAF and be used to fit the observed data. In this

model, the radio emission is generated by synchrotron radiation from thermal electrons.

The parameters used to characterize the ADAF model include the scaled black hole mass m, scaled accretion rate $\dot{m}$, viscosity parameter α, ratio of gas pressure to total pressure β, and fraction of viscous energy transferred to electrons δ. The black hole mass ($m = 4.5 \times 10^9$; Shen & Gebhardt 2010) and accretion rate ($\dot{m} \sim 1.1 \times 10^{-8}$, averaged from two independent measurements; Johannsen et al. 2012; Paggi et al. 2014) were determined by observations and kept constant. The other three parameters α, β, and δ, were allowed to vary in order to fit the radio continuum spectrum of M60. We tried to fit the data with the Mahadevan (1997) model and found that the low-frequency band could not be accurately modeled because the observed spectral index $\alpha_{\rm thick} \sim 0.12$ was not consistent with the ADAF model. Therefore, a simple ADAF model with only thermal electrons cannot fully explain the observed radio spectrum of M60.

We included a BPL component in the model to refine the fit of the low-frequency data. This BPL component has the same expression as Equation (1) but allows for a negative value for $\alpha_{\rm thick}$, that is, a flat spectrum. The fitting results yielded the following parameters: $\alpha = 2.4^{+1.7}_{-1.1} \times 10^{-4}$, $\beta = 0.96^{+0.01}_{-0.03}$, $\delta = 0.61^{+0.25}_{-0.30}$, $\nu_{\rm t}^{\rm BPL} = 17.4^{+8.9}_{-7.9}$ GHz, $S_{\rm t}^{\rm BPL} = 4.3^{+1.2}_{-1.2}$ mJy, $\alpha_{\rm thick}^{\rm BPL} = -0.13^{+0.09}_{-0.13}$, and $\alpha_{\rm thin}^{\rm BPL} = -1.3^{+0.2}_{-0.4}$. The fitting results are shown in Figure 3 (top right).

The BPL component can be attributed to the synchrotron radiation of nonthermal electrons in the ADAF (Özel et al. 2000; Yuan et al. 2003; Bandyopadhyay et al. 2019; Cho et al. 2022). This further indicates that the core size at lower frequencies is larger than the pure thermal electron model. Moreover, the core size versus frequency relation is more complicated, and no straightforward solution can be derived. Therefore, we have only plotted the core size versus frequency relation for the pure thermal electron model, considering it as a lower bound (Figure 3 bottom).

3.3. New Evidence for the Existence of an SMBH in M60

The stellar dynamics (Shen & Gebhardt 2010) and X-ray hot gas hydrodynamics (Humphrey et al. 2008; Paggi et al. 2014, 2017) of M60 suggest the presence of a massive dark object at its center. This could be an SMBH or a cluster of brown dwarfs or stellar remnants (Maoz 1995, 1998). Here, we present a new argument in favor of the central massive object being an SMBH. Previous studies have demonstrated that if the maximum lifetime of a putative dark cluster is much less than the age of the host galaxy, due to evaporation and physical collision, it could not survive to the present (Maoz 1995, 1998; Genzel et al. 2000; Ghez et al. 2005; Shen et al. 2005). With a black hole mass of $4.5 \times 10^9\,M_\odot$ and a core size at 7.6 GHz of 0.27 mas, the half-mass density of the central object is $\rho_{\rm h} \geqslant 5.4 \times 10^{13}\,M_\odot\,{\rm pc}^{-3}$. If the central object is a dark cluster, its lifetime would be $\tau \leqslant 8.4 \times 10^9$ yr, which is less than the lifetime of the host galaxy, $\sim 10^{10}$ yr (see Figure 4 and the detailed calculation method presented in Appendix C). Therefore, it is more likely that the centiparsec-scale radio core in M60 is associated with an SMBH.

Johannsen & Psaltis (2010) proposed a method to estimate the mass of the SMBH by imaging its compact radio structure with VLBI. They showed that the light around the SMBH form a ringlike structure, its diameter is determined by the mass of the SMBH ($d_{\rm ring} = 5.2\,R_{\rm S}$) and are not significantly affected by the spin of the SMBH, the angle of inclination, or the observation frequency. Thus, the mass of the SMBH can be estimated by the size of the associated compact radio source. Taking the core size of M60 at 7.6 GHz ($\theta_{\rm size} \leqslant 0.27$ mas) as the upper limit of the photon ring diameter, an upper limit for the SMBH mass can be derived: $M_{\rm BH} \leqslant 4.3 \times 10^{10}\,M_\odot$. This independent derived upper limit for the black hole mass is consistent with the mass determined by stellar dynamics ($(4.5 \pm 1.0) \times 10^9 M_\odot$; Shen & Gebhardt 2010) and estimated from X-ray hot gas hydrodynamics ($(5.1 \pm 0.9) \times 10^9 M_\odot$; Humphrey et al. 2008; Paggi et al. 2014, 2017).

4. Conclusions

We presented high-resolution VLBA observations conducted in snapshot mode at 4.4 and 7.6 GHz alongside radio flux density data that include low-resolution data. The resulting VLBA image revealed compact components with a flux density of 19.1 ± 1.0 mJy at 4.4 GHz and 20.2 ± 1.0 mJy at 7.6 GHz. The size of the components, estimated by MCMC fitting, was $\leqslant 83$ $R_{\rm S} = 0.036$ pc $= 0.45$ mas at 4.4 GHz and $\leqslant 50$ $R_{\rm S} = 0.022$ pc $= 0.27$ mas at 7.6 GHz. The brightness temperature of the compact components in both bands was $T_{\rm B} \geqslant 6 \times 10^9$ K. The multiband radio flux density of M60 displayed a peaked spectrum. These results enable us to confidently identify the compact component as the radio core of M60. The radio core detected by VLBA within M60 could be due to synchrotron radiation of nonthermal electrons in the jet base, or it could also be attributed to synchrotron radiation generated by a combination of thermal and nonthermal electrons present within ADAF. The high mass density ($\rho_{\rm h} \geqslant 5.4 \times 10^{13}\,M_\odot\,{\rm pc}^{-3}$) suggests that the central object is an SMBH rather than a dark cluster. The black hole mass was restricted to $M_{\rm BH} \leqslant 4.3 \times 10^{10}\,M_\odot$, which is in agreement with the dynamical mass.

Our findings indicate that M60 could be a promising object for further deep VLBI observations at $\geqslant$15 GHz. This would enable us to accurately determine the diameter of the potential photon ring and the mass of its SMBH, as well as to investigate the jet base and ADAF in M60. We have been granted permission for 16 Gbps observations on M60 at 22 and 43 GHz using the Korean VLBI Network and some stations in the European VLBI Network. This project is scheduled to be observed in the near future.

Acknowledgments

This work is supported by the National Natural Science Foundation of China (No. 12203014). X.-P.C. was supported by the Brain Pool Program through the National Research Foundation of Korea (NRF) funded by the Ministry of Science and ICT (2019H1D3A1A01102564). We thank Feng Wang, Ying Mei, and Hui Deng for their insightful discussions during the initial stages of our work. This research has made use of the NASA/IPAC Extragalactic Database (NED), which is operated by the Jet Propulsion Laboratory, California Institute of Technology, under contract with the National Aeronautics and Space Administration. The National Radio Astronomy Observatory is a facility of the National Science Foundation operated under cooperative agreement by Associated Universities, Inc. This paper makes use of the following ALMA data: ADS/JAO.ALMA#2016.1.01135.S and ADS/JAO.ALMA#2017.1.00830.S. ALMA is a partnership of ESO (representing

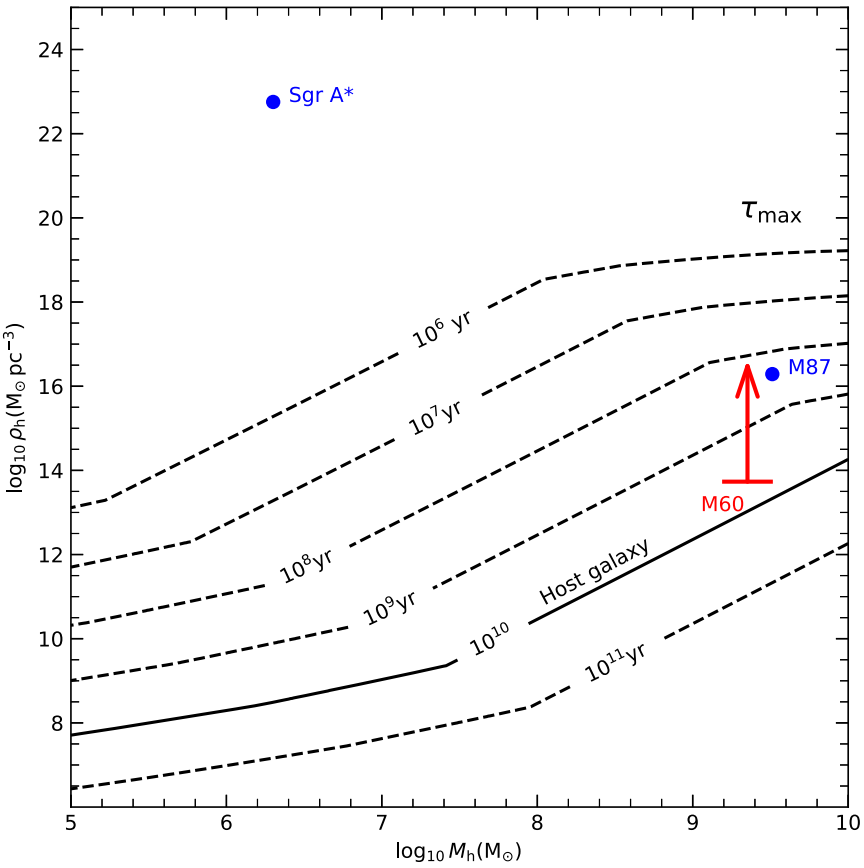

Figure 4. The maximum potential life span of a dark cluster with half-mass M_h and half-mass density ρ_h. The red data point represents M60 from this work, while the blue data points denote M87 (EHT Collaboration et al. 2019) and Sgr A* (EHT Collaboration et al. 2022). The life span of the hypothetical dark cluster in M60 is less than 10 Gyr, suggesting that the central object is an SMBH.

its member states), NSF (USA) and NINS (Japan), together with NRC (Canada), MOST and ASIAA (Taiwan), and KASI (Republic of Korea), in cooperation with the Republic of Chile. The Joint ALMA Observatory is operated by ESO, AUI/NRAO and NAOJ.

Facilities: VLBA (NRAO), VLA (NRAO), ALMA.

Software: AIPS (Greisen 2003), CASA (McMullin et al. 2007), Difmap (Shepherd 1997), DiFX (Deller et al. 2011), MCMCUVFit, Astropy (Astropy Collaboration et al. 2018).

Appendix A
Gain Correction Factors for Amplitude Self-calibration

Table 3 shows the gain correction factors of the 1241+166 and M60. After applying the gain correction factors of amplitude calibrator 1241+166 to the target source M60, the gain correction factors of M60 are close to 1, which indicates the amplitude of M60 data calibrated well.

Table 3
Gain Correction Factors of Amplitude Calibrator 1241+166 and Target Source M60

IF	BR	FD	HN	LA	MK	OV	SC	IF	BR	FD	HN	LA	MK	OV	SC
			1241+166 at 4.4 GHz								M60 at 4.4 GHz				
1	1.04	1.03	0.94	1.30	0.88	0.88	1.00	1	0.96	0.97	1.01	1.02	1.01	1.04	1.04
2	0.85	0.98	0.96	1.25	0.92	0.97	1.03	2	1.01	0.97	0.99	0.98	0.98	1.03	1.01
3	0.92	0.88	0.94	1.22	0.84	0.93	1.09	3	0.98	0.95	1.02	1.01	0.98	1.02	0.98
4	1.00	0.86	0.86	1.11	0.79	0.93	0.99	4	1.03	1.02	0.95	1.05	0.97	1.03	0.90
			1241+166 at 7.6 GHz								M60 at 7.6 GHz				
1	1.04	0.87	1.03	0.90	0.96	1.12	1.03	1	0.99	0.98	1.04	1.00	1.04	1.03	0.90
2	0.97	0.91	1.10	0.96	0.99	0.99	0.99	2	1.02	0.99	1.10	0.90	1.02	0.99	1.05
3	1.03	1.06	0.93	0.91	0.84	0.96	1.09	3	0.97	0.97	0.92	1.06	1.02	0.97	1.00
4	1.04	0.94	1.04	0.92	0.99	1.07	0.93	4	1.01	1.01	1.02	1.04	0.93	1.01	1.03

Appendix B
MCMC Fitting

To derive the total flux density ($S_{\rm tot}$), core size ($\theta_{\rm core}$), and relative position (x, y) of M60, we fitted the calibrated visibility data using the MCMC method, as recommended by Salafia et al. (2022). The logarithmic likelihood equation used in the fitting is

$$\ln L(x) = -\frac{1}{2}\Sigma_{i=0}^{N} w_i[(V_{R,m}(u_i, v_i, \theta) - V_{R,i})^2 + (V_{I,m}(u_i, v_i, \theta) - V_{I,i})^2], \quad \text{(B1)}$$

where $V_{R,i}$ and $V_{I,i}$ represent the real and imaginary parts of the ith visibility at the position (u_i, v_i), and w_i is data weight. $V_{R,m}(u, v, \theta)$ and $V_{I,m}(u, v, \theta)$ are the real and imaginary parts of the model visibility, where $\theta = (S_{\rm tot}, \theta_{\rm core}, x, y)$ are parameters to be estimated. The model visibility function is defined as

$$V_{\rm m} = S_{\rm tot} \exp\left[-2\pi^2\left(\frac{\theta_{\rm core}}{\sqrt{8\ln 2}}\right)^2 (u^2 + v^2) - 2\pi i(ux + vy)\right], \quad \text{(B2)}$$

where $i = \sqrt{-1}$.

The MCMC fitting was executed using MCMCUVFit, a Python-based software specifically designed for fitting visibility data using the MCMC method. The input model for MCMC fitting needs four parameters: $S_{\rm tot}$, $\theta_{\rm core}$, x, and y. The search ranges for these four parameters to be estimated were set as follows: 10–25 mJy for $S_{\rm tot}$, 10^{-6}–2 mas for $\theta_{\rm core}$, and −1 to 1 mas for both x and y. The MCMC fitting process was conducted with 200 walkers and 10^4 iterations. The initial half of the samples were discarded, and results are presented using corner plots in Figure 5. The parameters fitted through this process are listed in Table 1.

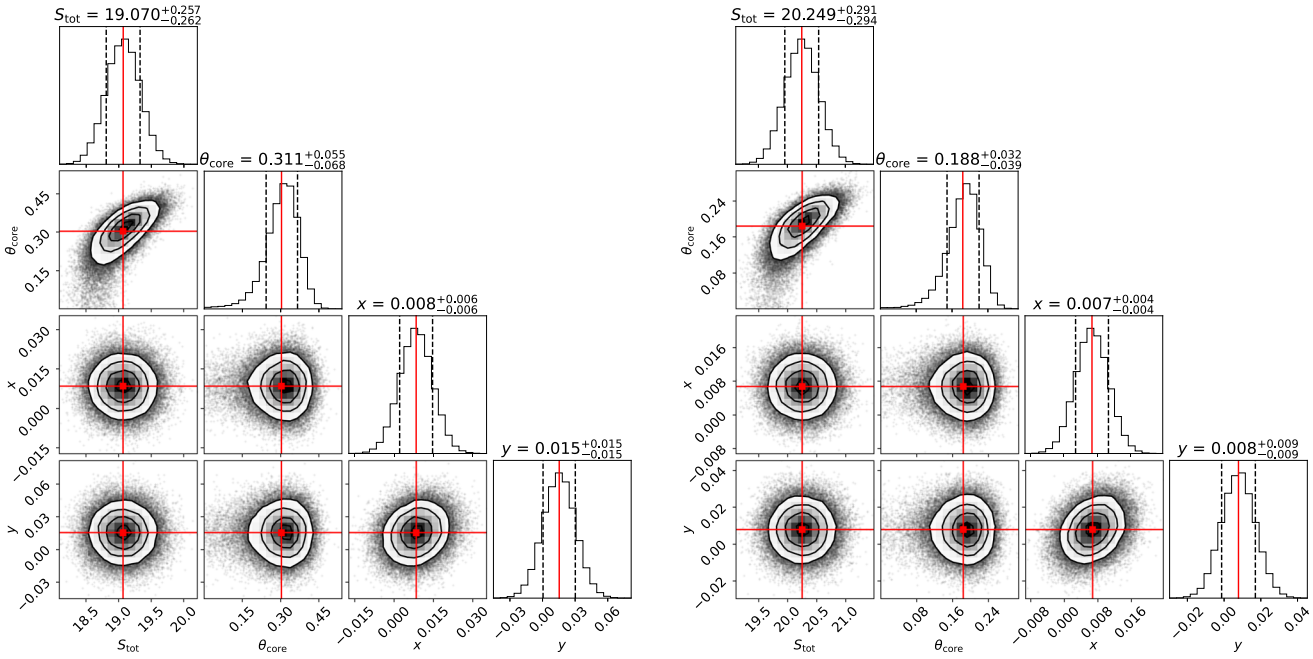

Figure 5. Corner plots of the circular Gaussian model fitting results for VLBA visibility data (left for 4.4 GHz and right for 7.6 GHz). There were 10,000 MCMC simulations in the plot. The red lines represent the medians. The four parameters are total flux density in mJy, core size in mas, and x- and y-coordinates in mas.

Appendix C
Lifetime of the Dark Cluster

Our approach to estimating the lifetime of the dark cluster present here follows Maoz (1995, 1998, and references therein). Since our objective is to exclude a dark cluster by illustrating that its lifetime is very short, we only consider the cluster that could survive for a long time. We presuppose that the structure of the cluster is described by the Plummer model, with each constituent object assumed to have the same mass and zero temperature.

The dark cluster could be composed of a variety of objects, such as (1) black holes with $m_* \geqslant 3\,M_\odot$, (2) neutron stars with $1.4\,M_\odot \leqslant m_* \leqslant 3\,M_\odot$, (3) brown dwarfs, and (4) white dwarfs with $10^{-3}\,M_\odot \leqslant m_* \leqslant 1.4\,M_\odot$. The life span of a cluster is determined by the mass and radius of the objects that constitute it. We use R_S to represent the black hole radius. The radius of a neutron star is given by the equation

$$r_*(m_*) = \frac{(18\pi)^{2/3}}{10}\frac{\hbar^2}{Gm_*^{1/3}}\left(\frac{1}{m_H}\right)^{8/3}, \tag{C1}$$

where $\hbar$ is the Plank constant and m_H is the mass of the hydrogen atom. The radius of a white dwarf at zero temperature is expressed by the formula

$$r_*(m_*) = \frac{1.57\times 10^9}{\mu}\frac{[1-(m_*/M_3)^{4/3}]^{1/2}}{(m_*/M_3)^{1/2}}\ \mathrm{cm}, \tag{C2}$$

where μ is the mean molecular weight and $M_3 = 5.816\,\mu^{-2}\,M_\odot$. Lastly, the radius of a brown dwarf is represented by

$$r_*(m_*) = 2.2\times 10^9\left(\frac{m_*}{M_\odot}\right)^{-1/3} \times\left[1+\left(\frac{m_*}{0.0032\,M_\odot}\right)^{-1/2}\right]^{-4/3}\ \mathrm{cm}. \tag{C3}$$

The lifetime of a dark cluster is constrained by two processes: evaporation and physical collisions. The maximum possible lifetime of the dark cluster depends on the cluster's half-mass $M_h \equiv M/2$ and its half-mass density ρ_h, where M is the mass of the cluster. The evaporation process is a consequence of weak gravitational scattering. The evaporation timescale of a cluster can be described as follows:

$$t_{evap} \simeq \frac{4.3\times 10^4 (M_h/m_*)}{\ln[0.8(M_h/m_*)]}\left(\frac{\rho_h}{10^8 M_\odot\ \mathrm{pc}^{-3}}\right)^{-1/2}\ \mathrm{yr}. \tag{C4}$$

The typical timescale for each object to physically collide with another is given by

$$t_{coll}(r_*, r_*) = \left[23.8 G^{1/2} M_h^{1/3}\rho_h^{7/6}\left(\frac{r_*^2}{m_*}\right)\left(1+\frac{m_*}{2^{1/2}\rho_h^{1/3}M_h^{2/3}r_*}\right)\right]^{-1}\ \mathrm{s}. \tag{C5}$$

For a given M_h and ρ_h, the lifetime of a cluster composed of objects with mass m_* and radius r_* is

$$\tau(r_*, m_*) = \min[t_{coll}, t_{evap}]. \tag{C6}$$

The maximum lifetime of a dark cluster, τ_{max}, can be determined by examining all classes of dark objects mentioned above across different mass ranges, i.e.,

$$\tau_{max}(M_h, \rho_h) = \max[\tau(r_*, m_*)]. \tag{C7}$$

Figure 4 shows the τ_{max} for each pair of M_h and ρ_h.

ORCID iDs

Xiaofeng Li https://orcid.org/0000-0002-9093-6296
Jun Yang https://orcid.org/0000-0002-2322-5232
Xiaopeng Cheng https://orcid.org/0000-0003-4407-9868
Mai Liao https://orcid.org/0000-0002-9137-7019
Xiaoyu Hong https://orcid.org/0000-0002-1992-5260
Liming Dou https://orcid.org/0000-0002-4757-8622
Fupeng Zhang https://orcid.org/0000-0002-0403-9522
Weirong Huang https://orcid.org/0000-0001-8449-6020

References

ALMA Pipeline Team 2017, ALMA Science Pipeline User's Guide, ALMA Doc 5.13
Anderson, J. M., Ulvestad, J. S., & Ho, L. C. 2004, ApJ, 603, 42
Astropy Collaboration, Price-Whelan, A. M., Sipőcz, B. M., et al. 2018, AJ, 156, 123
Bandyopadhyay, B., Xie, F.-G., Nagar, N. M., et al. 2019, MNRAS, 490, 4606
Blandford, R. D., & Begelman, M. C. 1999, MNRAS, 303, L1
Blandford, R. D., & Payne, D. G. 1982, MNRAS, 199, 883
Blandford, R. D., & Znajek, R. L. 1977, MNRAS, 179, 433
Bower, G. C., Goss, W. M., Falcke, H., Backer, D. C., & Lithwick, Y. 2006, ApJL, 648, L127
Callingham, J. R., Ekers, R. D., Gaensler, B. M., et al. 2017, ApJ, 836, 174
Cantiello, M., Blakeslee, J. P., Ferrarese, L., et al. 2018, ApJ, 856, 126
Capetti, A., Brienza, M., Balmaverde, B., et al. 2022, A&A, 660, A93
Chen, L. 2017, ApJ, 842, 129
Chen, L., & Zhang, B. 2021, ApJ, 906, 105
Cheng, X., Cho, I., Kawashima, T., et al. 2023, Galax, 11, 46
Cho, I., Zhao, G.-Y., Kawashima, T., et al. 2022, ApJ, 926, 108
Crossley, J. H., Sjouwerman, L. O., Fomalont, E. B., & Radziwill, N. M. 2008, Proc. SPIE, 7016, 70160O
Deller, A. T., Brisken, W. F., Phillips, C. J., et al. 2011, PASP, 123, 275
Di Matteo, T., & Fabian, A. C. 1997, MNRAS, 286, L50
Di Matteo, T., Fabian, A. C., Rees, M. J., Carilli, C. L., & Ivison, R. J. 1999, MNRAS, 305, 492
Doi, A., Kameno, S., & Inoue, M. 2005, MNRAS, 360, 119
Dunn, R. J. H., Allen, S. W., Taylor, G. B., et al. 2010, MNRAS, 404, 180
EHT Collaboration, Akiyama, K., Alberdi, A., et al. 2019, ApJL, 875, L1
EHT Collaboration, Akiyama, K., Alberdi, A., et al. 2022, ApJL, 930, L12
Falcke, H., & Biermann, P. L. 1999, A&A, 342, 49
Falcke, H., Nagar, N. M., Wilson, A. S., & Ulvestad, J. S. 2000, ApJ, 542, 197
Fanaroff, B. L., & Riley, J. M. 1974, MNRAS, 167, 31P
Gaia Collaboration, Vallenari, A., Brown, A. G. A., et al. 2023, A&A, 674, A1
Gebhardt, K., Bender, R., Bower, G., et al. 2000, ApJL, 539, L13
Genzel, R., Pichon, C., Eckart, A., Gerhard, O. E., & Ott, T. 2000, MNRAS, 317, 348
Ghez, A. M., Salim, S., Hornstein, S. D., et al. 2005, ApJ, 620, 744
Greisen, E. W. 2003, in Information Handling in Astronomy—Historical Vistas, ed. A. Heck, Vol. 285 (Dordrecht: Springer), 109
Grossová, R., Werner, N., Massaro, F., et al. 2022, ApJS, 258, 30
GRAVITY Collaboration, Abuter, R., Amorim, A., et al. 2019, A&A, 625, L10
Hada, K., Doi, A., Kino, M., et al. 2011, Natur, 477, 185
Hada, K., Doi, A., Nagai, H., et al. 2013, ApJ, 779, 6
Ho, L. C. 2008, ARA&A, 46, 475
Ho, L. C., Filippenko, A. V., & Sargent, W. L. W. 1997, ApJ, 487, 568
Ho, L. C., & Ulvestad, J. S. 2001, ApJS, 133, 77
Humphrey, P. J., Buote, D. A., Brighenti, F., Gebhardt, K., & Mathews, W. G. 2008, ApJ, 683, 161
Janssen, M., Falcke, H., Kadler, M., et al. 2021, NatAs, 5, 1017
Jiang, W., Shen, Z., Jiang, D., Martí-Vidal, I., & Kawaguchi, N. 2018, ApJL, 853, L14
Jiang, W., Shen, Z., Martí-Vidal, I., et al. 2021, ApJL, 922, L16
Johannsen, T., & Psaltis, D. 2010, ApJ, 718, 446
Johannsen, T., Psaltis, D., Gillessen, S., et al. 2012, ApJ, 758, 30
Kharb, P., O'Dea, C. P., Baum, S. A., et al. 2014, MNRAS, 440, 2976

Kharb, P., O'Dea, C. P., Baum, S. A., Colbert, E. J. M., & Xu, C. 2006, ApJ, 652, 177
Konigl, A. 1981, ApJ, 243, 700
Kormendy, J., & Ho, L. C. 2013, ARA&A, 51, 511
Koryukova, T. A., Pushkarev, A. B., Plavin, A. V., & Kovalev, Y. Y. 2022, MNRAS, 515, 1736
Lee, M. G., & Jang, I. S. 2017, ApJ, 841, 23
Lister, M. L., Homan, D. C., Kellermann, K. I., et al. 2021, ApJ, 923, 30
Lo, W.-P., Asada, K., Matsushita, S., et al. 2023, ApJ, 950, 10
Lu, R.-S., Asada, K., Krichbaum, T. P., et al. 2023, Natur, 616, 686
Lu, R.-S., Krichbaum, T. P., Roy, A. L., et al. 2018, ApJ, 859, 60
Mahadevan, R. 1997, ApJ, 477, 585
Manmoto, T., Mineshige, S., & Kusunose, M. 1997, ApJ, 489, 791
Maoz, E. 1995, ApJL, 447, L91
Maoz, E. 1998, ApJL, 494, L181
McMullin, J. P., Waters, B., Schiebel, D., Young, W., & Golap, K. 2007, in ASP Conf. Ser. 376, Astronomical Data Analysis Software and Systems XVI, ed. R. A. Shaw, F. Hill, & D. J. Bell (San Francisco, CA: ASP), 127
Miyoshi, M., Moran, J., Herrnstein, J., et al. 1995, Natur, 373, 127
Nagar, N. M., Falcke, H., & Wilson, A. S. 2005, A&A, 435, 521
Nagar, N. M., Falcke, H., Wilson, A. S., & Ulvestad, J. S. 2002, A&A, 392, 53
Narayan, R., & Yi, I. 1994, ApJL, 428, L13
Narayan, R., & Yi, I. 1995, ApJ, 444, 231
Özel, F., Psaltis, D., & Narayan, R. 2000, ApJ, 541, 234
Paggi, A., Fabbiano, G., Kim, D.-W., et al. 2014, ApJ, 787, 134
Paggi, A., Kim, D.-W., Anderson, C., et al. 2017, ApJ, 844, 5
Panessa, F., Baldi, R. D., Laor, A., et al. 2019, NatAs, 3, 387
Park, S., Yang, J., Oonk, J. B. R., & Paragi, Z. 2017, MNRAS, 465, 3943
Psaltis, D., Johnson, M., Narayan, R., et al. 2018, arXiv:1805.01242
Pushkarev, A. B., Kovalev, Y. Y., Lister, M. L., & Savolainen, T. 2017, MNRAS, 468, 4992
Ramakrishnan, V., Nagar, N., Arratia, V., et al. 2023, Galax, 11, 15
Rauch, C., Ros, E., Krichbaum, T. P., et al. 2016, A&A, 587, A37
Salafia, O. S., Ravasio, M. E., Yang, J., et al. 2022, ApJL, 931, L19
Shen, J., & Gebhardt, K. 2010, ApJ, 711, 484
Shen, Z.-Q., Lo, K. Y., Liang, M. C., Ho, P. T. P., & Zhao, J. H. 2005, Natur, 438, 62
Shepherd, M. C. 1997, in ASP Conf. Ser. 125, Astronomical Data Analysis Software and Systems VI, ed. G. Hunt & H. Payne (San Francisco, CA: ASP), 77
Shurkin, K., Dunn, R. J. H., Gentile, G., Taylor, G. B., & Allen, S. W. 2008, MNRAS, 383, 923
Stanger, V. J., & Warwick, R. S. 1986, MNRAS, 220, 363
Temi, P., Gaspari, M., Brighenti, F., et al. 2022, ApJ, 928, 150
Ulvestad, J. S., & Ho, L. C. 2001, ApJ, 558, 561
Ulvestad, J. S., Wrobel, J. M., Roy, A. L., et al. 1999, ApJL, 517, L81
Yuan, F., Quataert, E., & Narayan, R. 2003, ApJ, 598, 301